Forward Brillouin scattering in hollow-core photonic bandgap fibers

2016 New J. Phys. 18 025008

(http://iopscience.iop.org/1367-2630/18/2/025008)

New Journal of Physics
The open access journal at the forefront of physics

Deutsche Physikalische Gesellschaft DPG
IOP Institute of Physics

Published in partnership with: Deutsche Physikalische Gesellschaft and the Institute of Physics

OPEN ACCESS

RECEIVED
11 November 2015

REVISED
18 December 2015

ACCEPTED FOR PUBLICATION
13 January 2016

PUBLISHED
5 February 2016

PAPER

Forward Brillouin scattering in hollow-core photonic bandgap fibers

W H Renninger[1], **H Shin, R O Behunin, P Kharel, E A Kittlaus and P T Rakich**

Department of Applied Physics, Yale University, New Haven, Connecticut 06520, USA
[1] Author to whom any correspondence should be addressed.

E-mail: william.renninger@yale.edu **and** peter.rakich@yale.edu

Keywords: hollow-core fiber, brillouin scattering, photonic bandgap fiber

Abstract

We quantify the strength of stimulated forward Brillouin scattering in hollow-core photonic bandgap fiber through a combination of experiments and multi-physics simulations. Brillouin spectroscopy methods reveal a family of densely spaced Brillouin-active phonon modes below 100 MHz with coupling strengths that approach those of conventional silica fiber. The experimental results are corroborated by multi-physics simulations, revealing that relatively strong optomechanical coupling is mediated by a combination of electrostriction and radiation pressure within the nano-scale silica-air matrix; the nontrivial mechanical properties of this silica-air matrix facilitate the large optomechanical response produced by this system. Simulations also reveal an incredible sensitivity of the Brillouin spectrum to fiber critical dimensions, suggesting opportunity for enhancement or suppression of these interactions. Finally, we relate the measured and calculated couplings to the noise properties of the fiber as the foundation for phase- and polarization-noise estimates in hollow-core fiber. More generally, such Brillouin interactions are an important consideration in both the high and low optical intensity limits.

1. Introduction

In contrast to conventional step-index fibers, hollow-core photonic bandgap fibers (HC-PBF) produce guidance of light in air through Bragg reflection from a periodic silica-air matrix [1–3]. This unique form of guidance has enabled powerful new opportunities for both classical and quantum applications. In the classical limit, reduced interaction of light with the silica-air matrix greatly reduces nonlinearities, enabling high power laser delivery [4] and new forms of optical pulse compression [5]. Infiltration of these hollow core fibers with atomic vapors and liquids radically enhances light-matter coupling as the basis for a diversity of new light sources [6]. In the quantum limit, strong coupling to atomic vapors, enabled by hollow-core fibers, has brought new concepts for single photon nonlinearities and interactions [7–10], including switching and memories [11]. Such applications require reduced interactions with the silica-air matrix, as both stimulated and spontaneous light scattering processes adversely impact quantum coherence [12–20]. While Kerr and Raman nonlinearities are greatly suppressed in such fibers [1–3], little is known about the nature of third-order Brillouin interactions (resonant light-sound coupling), and the implications they could have in both low and high optical power limits.

In the high-field limit, strong coupling between guided photons and phonons produces Brillouin-based amplification of light within solid core fibers [21, 22]. In the weak-field limit, this same interaction produces incoherent light scattering processes that corrupt quantum coherence [12–20]. For instance, spontaneous forward-Brillouin interactions (also termed guided-acoustic wave Brilloiun scattering, or GAWBS [23, 24]) pose a fundamental limitation for fiber-based generation of nonclassical light in silica fibers [12–20]. More recently, hollow-core fibers have been used to achieve strong coupling with atomic vapors for a range of quantum information processing schemes [7–11]. Owing to the reduced interaction of light with the silica-air matrix of a HC-PBF, one might expect Brillouin noise to be negligible in these systems. However, the observation of excess noise at frequencies consistent with acoustic phonons raises important questions about the strength and nature of Brillouin interactions in hollow-core fibers [25]. While the phase matching considerations for this process are

identical to those of solid-core fibers, the nature of the optomechanical coupling within the nanomechanical silica-air matrix is far more complex, making the mastery of such interactions in HC-PBF very challenging.

In this paper, we quantify the strength of photon–phonon coupling in HC-PBF for the first time through a combination of experiment and theory, revealing a range of nontrivial optomechanical interactions mediated by the nano-scale silica-air matrix. Using a sensitive stimulated inter-polarization forward Brillouin spectroscopy technique we measure the coupling strength and frequencies of forward Brillouin interactions; experiments reveal a densely spaced set of Brillouin-active phonon modes below 100 MHz with linewidths that increase monotonically with frequency. Surprisingly large forward-Brillouin coupling strengths (10^{-3} W^{-1} m^{-1}) are found, approaching the magnitudes of those of solid-core silica fibers (for example, forward Brillouin gain in SMF28 is $\sim 10^{-2}$ W^{-1} m^{-1}, as calculated in [21]). Measurements are corroborated through multi-physics simulations, revealing identifiably different types of Brillouin active phonon modes: those with high energy densities in the nanoscale silica-air matrix and extended phonon modes with energy distributed throughout the entire fiber cross-section. In addition, each mode type can have varying degrees of localization. Comparison of the Brillouin linewidths observed in air with those observed under vacuum reveals a clear (2.5-fold) change in phonon linewidth, providing strong evidence that the nanoscale silica-air matrix participates strongly in a subset of these phonon modes.

Computational studies also reveal incredible dimensional sensitivity of photon–phonon coupling, suggesting that a one-to-one mapping of simulated to observed Brillouin-active modes is difficult without extremely precise knowledge of the fiber dimensions along its entire length. Alternatively, these same simulations suggest that there is significant opportunity to either enhance or suppress photon–phonon coupling through small modifications in the fiber dimension. Through experiments, we show that the strength and character of the Brillouin response is very sensitive to the conditions of optical coupling, indicating the noise properties of this fiber can vary significantly without proper care.

Finally, we provide an analytical expression that relates the Brillouin coupling coefficients to the spontaneous Brillouin power-spectrum. That is, we illustrate that only the coupling strength, Brillouin linewidth, and temperature are needed to relate the Brillouin gain coefficient to the noise spectrum, in a general way. Thus, the forward Brillouin scattering limitation for both high power and noise sensitive applications is directly determined. Furthermore, new understanding of Brillouin interaction in HC-PBF may eventually find applications such as for frequency-comb generation, active phase modulation and high-harmonic mode-locking of lasers [22].

This paper is structured as follows. In section 2 we introduce the basic physics of stimulated Brillouin scattering in HC-PBF and describe the phonon-mediated four-wave mixing (Ph-FWM) processes that are used to quantify Brillouin interactions in HC-PBF. In sections 3, 4, we describe our experimental results, and quantify the strength of Brillouin coupling. In section 5, we develop multi-physics simulations and compare the simulated Brillouin couplings with the measured couplings. In section 6, we connect the experimental and theoretical results to spontaneous Brillouin scattering, and in section 7 we discuss the potential implications of our findings and conclude.

2. Forward Brillouin interactions in hollow core fiber

2.1. Stimulated forward Brillouin interactions

This paper explores forward Brillouin interactions in the hollow core photonic bandgap fiber of the type seen in figure 1(a) with a 1550 nm wavelength (for more on HC-PBF fibers of this type, see [1–3]). Through forward-Brillouin processes, resonant coupling between co-linearly propagating guided optical waves is mediated by a combination of material-induced electrostrictive forces and radiation pressure. Electrostrictive forces are derived from the photoelastic (or nonlinear) material response while radiation pressure forces are geometric in origin. These forces are generated according to the rules described in [26, 27] and are nonzero in the presence of a strong electric field, near the center of the hollow-core fiber (figure 1(b)). Radiation pressure produces surface pressure normal to the nano-web surfaces (at dielectric interfaces) and electrostrictive forces are expressed in the silica material and at surfaces. The complexity of the optical field and silica mesh translates to a highly nontrivial force distribution in the photonic bandgap fiber. For a monochromatic guided optical mode, these driving forces are almost completely transverse.

Through forward Brillouin processes, co-linearly propagating pump and Stokes waves with frequencies ω_1 and ω_2, respectively, couple through resonantly generated phonons of frequency difference $\Omega = \omega_1 - \omega_2$; interference between these waves drives the excitation of phonons. Phase matching requires $k(\omega_1) = K(\Omega) + k(\omega_2)$, where $k(\omega)$ and $K(\Omega)$ is the optical and phonon dispersion relations, respectively, as shown schematically in figure 1(d). The set of phonon modes $\{\Omega_i\}$ that are 'Brillouin-active' satisfy the condition $K(\Omega_i) = k(\omega_1) - k(\omega_1 - \Omega_i) \cong (\partial k/\partial\omega)\Omega_i = \Omega_i/v_g$, where v_g is the optical group velocity. Since

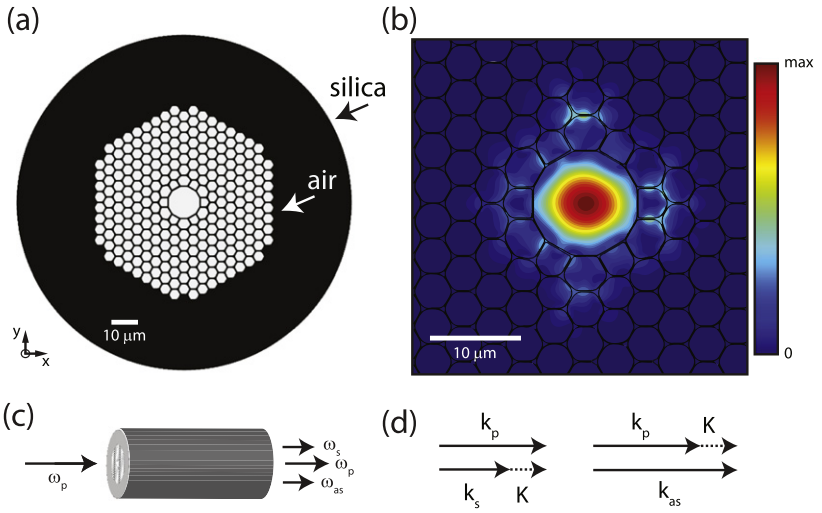

Figure 1. Hollow-core fiber (a) cross section and (b) near field intensity profile of the fundamental optical mode obtained by the simulation methods described in section 5. (c) Brillouin frequencies of interest in the HC-PBF, indicated as inputs and outputs. (d) Phase matching condition for the Stokes and anti-Stokes processes, respectively.

these Brillouin active phonon modes have an exceedingly small longitudinal wave-vector ($2\pi K^{-1} \sim 10$ m), they can, to an excellent approximation, be treated as transverse acoustic resonances at the phonon cutoff frequency (i.e., the $K = 0$ mode).

Depending on the symmetry of the phonon displacement field, the Brillouin active phonon mode can produce either intra-polarization or inter-polarization (depolarization) scattering [23, 24]. For intra-polarization scattering processes, the interacting pump and Stokes waves propagate in the same polarization mode, whereas through inter-polarization scattering the Brillouin active phonon mode couples optical modes of orthogonal polarizations. As in conventional silica fibers, both types of interactions are possible in the HC-PBF system under study.

Both interactions are diagrammed in figures 2(a), (b). Optical field amplitudes (A_k) of frequency ω_k and polarization state m are denoted as (ω_k, m), with associated guided power $P_k = |A_k|^2$. In the Stokes process diagramed in figures 2(a), (b), an incident pump-field (ω_1, p) transfers energy to a Stokes-field having similar (ω_2, p) or orthogonal (ω_2, s) polarization states through an intra- and inter-polarization process respectively. The coupling strength for intra-polarization coupling ($\|$) and inter-polarization coupling ($\perp$), is captured by the Brillouin gain coefficient, denoted as $G_i^{\|}$ and $G_i^{\perp}$ respectively; each gain coefficient is attributed to a phonon mode of frequency Ω_i. Resonant Brillouin coupling in the weak-signal limit produces a Stokes field (A_2) which grows according to $\mathrm{d}A_2/\mathrm{d}z = \gamma_i |A_1|^2 A_2$, where $\gamma_i = G_i/2$. Expressed in terms of power, $\mathrm{d}P_2/\mathrm{d}z = G_i P_1 P_2$, where $G_i \to G_i^{\|}$ for intra-polarization scattering and $G_i \to G_i^{\perp}$ for inter-polarization scattering. Note that the magnitude of $G_i^{\|/\perp}$ depends on the opto-mechanical coupling strength of the Brillouin-active phonon mode (equation (1)), which is related to the relative symmetries of the optical and acoustic modes.

2.2. Spontaneous forward Brillouin scattering

The underlying physics of spontaneous Brillouin interactions (also termed GAWBS) is very similar to that of stimulated Brillouin processes. In both instances, Brillouin active phonons mediate energy transfer. However, the active phonons are thermally populated (or thermally driven) in the spontaneous Brillouin processes (figures 3(a), (b)), whereas with stimulated Brillouin processes (figures 2(b), (c)) phonons are driven by optical forces. The phase matching conditions are identical for both processes (figure 1(d)). Additionally, the scattering rates for the spontaneous Brillouin scattering are expressed succinctly in terms of Brillouin gain coefficient as $\mathrm{d}P_{\mathrm{scat.}}/\mathrm{d}z = GP_{\mathrm{pump}}N(T)$, where $N(T)$ is a temperature dependent driving term; for further details, see section 6.

2.3. Phonon mediated four-wave mixing processes

In contrast to backward Brillouin processes, guided optical modes with a wide wavelength separation can interact with the same forward Brillouin active phonon mode. Since the optical group-velocity, v_g, changes very little with wavelength, the same phonon mode, of wave-vector $K_i = \Omega_i/v_g$, mediates coupling between disparate wavelengths, provided that $\Delta KL \cong (\partial^2 k/\partial\omega^2)\Delta\omega\Omega_i L = D_\lambda \Omega_i \Delta\lambda L \ll 1$. Here, L is the fiber length, D_λ is the group-velocity dispersion, and $\Delta\lambda$ is the difference in wavelength. For example, in a 1 m long segment of HC-PBF, $\Delta KL < 10^{-4}$ for any two wavelengths separated by 10 nm, near 1550 nm ($D_\lambda \sim 100$ ps nm^{-1} km^{-1} at

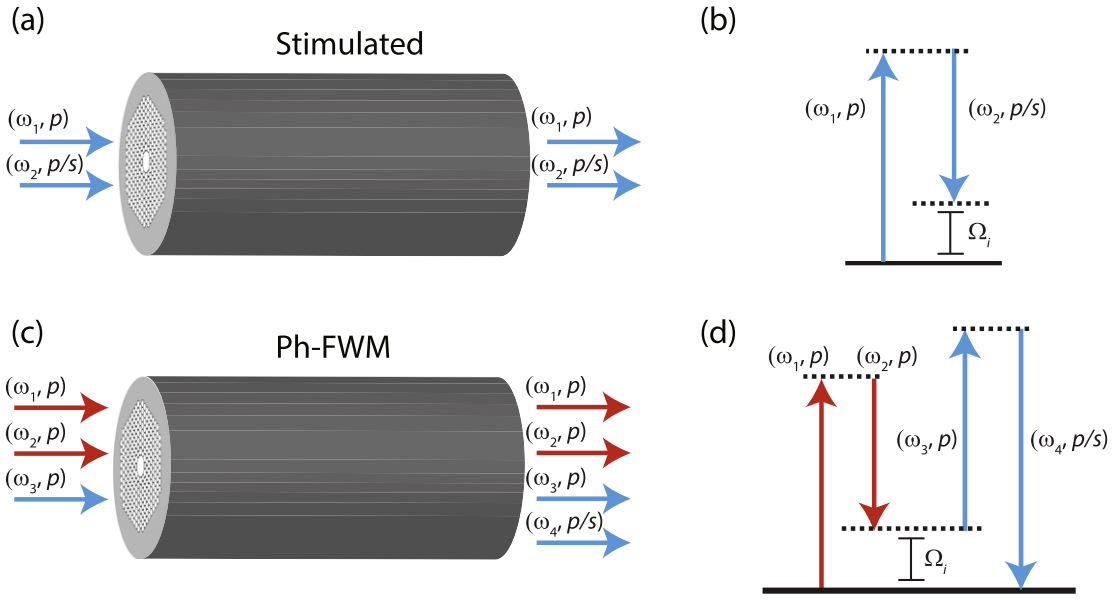

Figure 2. Hollow-core fiber with input and output fields and respective energy-level diagram for (a), (b) stimulated Stokes scattering process and (c), (d) the phonon mediated four-wave mixing process described in this work (both inter- or intra-polarized versions). Each frequency is indicated with a number and a polarization in parenthesis. Note that (c), (d) depicts one specific anti-Stokes interaction; the corresponding Stokes process occurs simultaneously.

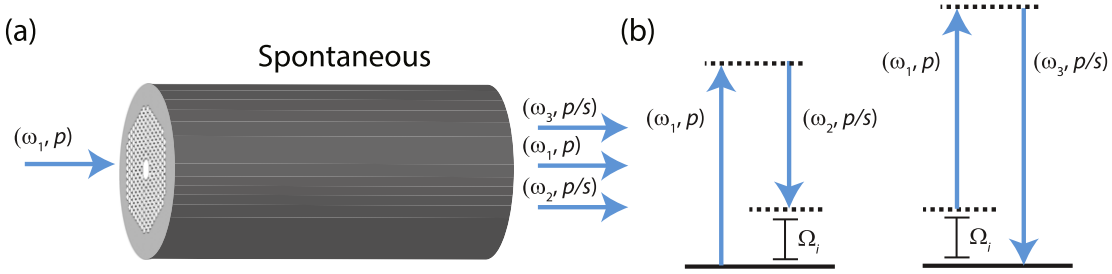

Figure 3. Hollow-core fiber with (a) input and output fields and (b) respective energy-level diagram for a spontaneous Stokes and anti-Stokes scattering process (polarized or depolarized GAWBS).

1550 nm wavelengths). As a consequence, the same phonon mode can be excited and probed through two-color Ph-FWM interactions (see figures 2(c), (d)) with negligible phase-mismatch.

One such Ph-FWM process is shown in figure 2(c). Through this interaction, two pump fields (ω_1, p) and (ω_2, p) resonantly drive a Brillouin-active phonon mode, while a probe field (ω_3, p) of a different color is used to read the excited phonon mode. Figure 2(d) shows a transition-diagram for a characteristic Ph-FWM processes. Through this interaction, the driven phonon mode scatters the probe field to a similar polarization (ω_4, p), or orthogonal polarization (ω_4, s) as seen in figure 2(c). In the weak-signal limit, a resonantly driven phonon mode, $\Omega_i = \omega_2 - \omega_1$, produces growth of the probe field (A_4) according to $dA_4/dz = \gamma_i A_1 A_2^* A_3$. Here $2\gamma_i \rightarrow [G_i^{\parallel} G_i^{\parallel}]^{1/2}$ for intra-polarization scattering and $2\gamma_i \rightarrow [G_i^{\parallel} G_i^{\perp}]^{1/2}$ for inter-polarization scattering; we refer to the former as co-polarized Ph-FWM and the latter as depolarized Ph-FWM. Note that while only the anti-Stokes process (ω_4, A_4) is diagrammed in figures 2(c), (d), the complementary Stokes process (ω_5, A_5) occurs simultaneously, with similar generation dynamics.

Exploiting the broadband nature of this interaction, phonon mediated four-wave mixing methods of the type described in [28, 29] are readily used to quantify the Brillouin coupling strength of isolated Brillouin resonances. Through these studies, co-polarized Ph-FWM was implemented, providing a sensitive method for detection of forward-Brillouin coupling in waveguides. However, through co-polarized Ph-FWM scattering measurements, Kerr induced four-wave mixing complicates the interpretation of densely spaced phonon resonances of the type observed in HC-PBF.

To avoid the problem of Kerr and Brillouin interference in HC-PBF, we perform depolarized (orthogonally polarized) Ph-FWM. This yields virtually background free measurements, permitting us to unambiguously

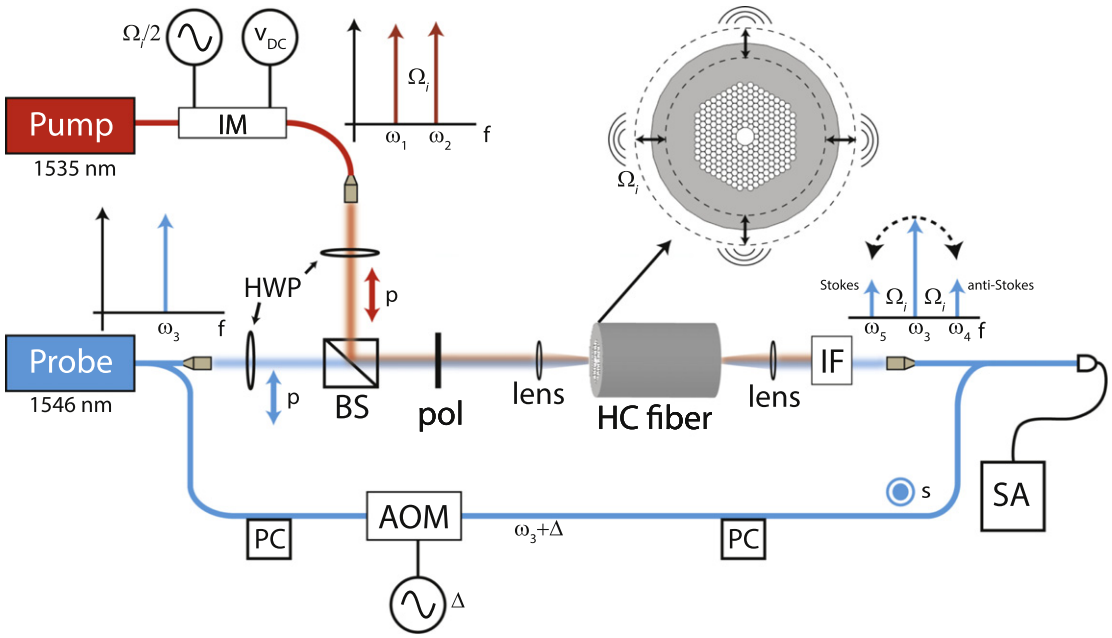

Figure 4. Experimental apparatus: IM, intensity modulator; HWP, half-wave plate; BS, 50:50 beamsplitter; HC fiber, hollow-core fiber; AOM, acousto-optic modulator; pol, polarizer; PC, polarization controller; IF, interference filter; and SA, spectrum analyzer. Ω_i is the acoustic resonance frequency. An AOM drive frequency (Δ) of 40 MHz is used. Co-polarization of the input frequencies is achieved with half-wave plates and a common polarizer. The polarization of the scattered waves is selected by appropriate polarization rotation of the AOM-shifted reference arm.

pinpoint the Brillouin interactions and quantify their coupling strength. Through these measurements we resonantly drive phonons with a modulated pump laser of $\lambda = 1535$ nm to synthesize pump tones (ω_1, p) and (ω_2, p), seen in figure 2(c). A co-linearly polarized probe beam at $\lambda = 1546$ nm is simultaneously injected into the fiber, corresponding to (ω_3, p). These driven Brillouin-active phonons scatter light from this probe beam to an orthogonal polarization state, (ω_4, s). Using additional polarization-based filtering, this signal wave is detected, permitting a nearly background-free measurement of photon–phonon coupling in HC-PBF.

As we will discuss further in section 5, silica fibers with perfect azimuthal symmetry will have a vanishing $G_i^{\parallel}G_i^{\perp}$, meaning that depolarized Ph-FWM also vanishes. However, the unique symmetry properties of the HC-PBF yield appreciable coupling through depolarized Ph-FWM. Through this interaction, the signal field (A_4) grows according to $\mathrm{d}A_4/\mathrm{d}z = [G_i^{\parallel}G_i^{\perp}]^{1/2}A_1A_2^*A_3/2$, where A_1, A_2, and A_3 are input drive-fields. For small values of A_4, the drive fields are approximately unchanged, meaning that at the output of a fiber segment of length L, the peak power scattered by the ith phonon modes is $P_4 = G_i^{\parallel}G_i^{\perp}L^2P_1P_2P_3/4$. In this way, our experiments allow us to quantify the magnitude of $G_i^{\parallel}G_i^{\perp}$ through depolarized Ph-FWM.

Through numerics, we show that the majority of Brillouin active phonon modes in HC-PBF produce strong depolarized Ph-FWM, meaning that these measurements provide a powerful new window into the stimulated Brillouin interactions in HC-PBF. We also show that the scattering rates for spontaneous Brillouin scattering are expressed succinctly in terms of these same gain coefficients, $G_i^{\parallel}$ and $G_i^{\perp}$ in section 6.

3. Stimulated Brillouin spectroscopy

A hybrid free-space and fiber apparatus is designed for sensitive measurement of depolarized phonon mediated four-wave mixing (see figure 4) [28, 30]. The two pump-fields (red), ω_1 and ω_2, are synthesized from a monochromatic laser line ($\lambda = 1535$ nm) using an intensity modulator. This is accomplished by biasing a Mach–Zehnder electro-optic modulator for maximum carrier suppression. The modulation frequency is swept through the Brillouin-active resonances producing a resonant excitation of phonons in the HC-PBF. A continuous-wave probe beam (blue), ω_3, is simultaneously injected into the fiber ($\lambda = 1546$ nm) with a 50:50 beam splitter, to permit detection of the excited phonons via Ph-FWM. Through this resonantly driven Brillouin scattering process, Stokes (ω_5) and anti-Stokes (ω_4) sidebands are imprinted on the probe beam (ω_3), as sketched in figure 4.

These Brillouin signatures (sidebands) are separated from the pump (red) using both spectral and polarization filtering before they are measured with heterodyne detection. The Stokes and anti-Stokes signals are

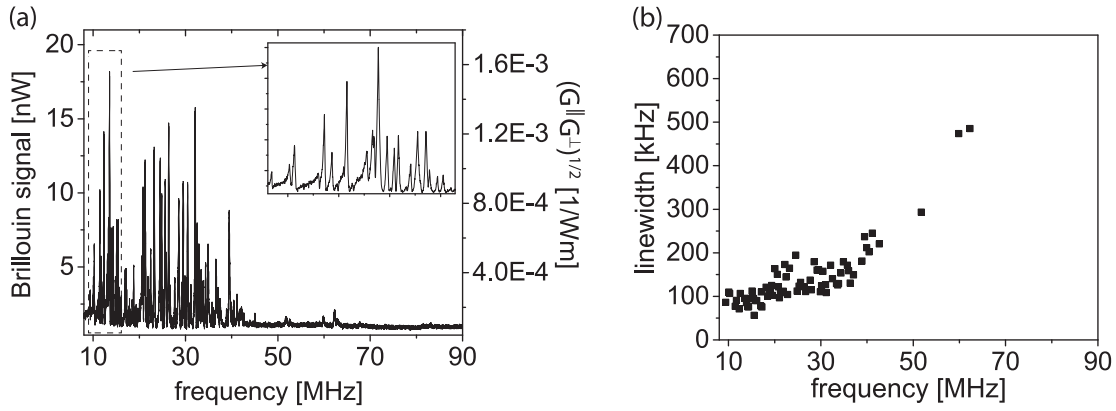

Figure 5. Ph-FWM forward Brillouin measurement results. (a) Measured signal power and Brillouin gain versus frequency. Inset: an enhanced view of the first few resonances. (b) Full-width at half-maximum linewidths of the identifiable resonances from (a).

detected at distinct frequencies by using an acousto-optic modulator (AOM) to synthesize a frequency-shifted local-oscillator. As shown in figure 4, probe laser light is frequency shifted from (ω_3) to ($\omega_3 + \Delta$) in the reference arm of the interferometer before it is combined with the generated signals at frequencies ω_4 and ω_5. The Stokes and anti-Stokes signals are then detected as beat-notes at frequencies ($\Omega_i - \Delta$) and ($\Omega_i + \Delta$) using a receiver. By tracking these distinct beat-notes as the drive frequency is swept, the Stokes or anti-Stokes Brillouin spectrum is measured versus frequency. Note that the Stokes and anti-Stokes Brillouin spectra contain identical information about the system. However, the use of a positive frequency shift from the AOM introduced an unwanted tone at the 40 MHz frequency of the AOM. To avoid this spurious tone, we show the Brillouin spectrum obtained by measuring the anti-Stokes Brillouin spectrum in figure 4.

Measurements reveal multiple closely spaced peaks below 100 MHz, which reduce in amplitude at higher frequencies (figure 5(a)). The linewidth of the resonances at the full width at half of the maximum power is shown to increase monotonically with frequency (figure 5(b)). The quality factor near 50 MHz, or $f/\Delta f$, is 200. With the known powers, fiber length, and coupling factor, the measured signal can be related to the nonlinear Brillouin gain, $\sqrt{G_i^{\parallel}G_i^{\perp}}$. When coupled with the AOM shifted reference signal, the measured heterodyne signal is given by $P_{\text{signal}} = 2\eta\sqrt{P_4 P_{\text{AOM}}} = L\sqrt{G_i^{\parallel}G_i^{\perp}}\,\eta\sqrt{P_1 P_2 P_3 P_{\text{AOM}}}$, where P_{AOM} is the optical power in the AOM arm; here η is a unitless scale-factor that accounts for the experimental losses produced by numerous fiber components in the optical path between the fiber segment and the detector. This coefficient was obtained through careful calibration of this apparatus using reference signals of known powers. Given $P_1 = P_2 = 42$ mW, $P_3 = 6.6$ mW, $P_{\text{AOM}} = 0.76$ mW, $L = 1.61$ m and $\eta = 7.6 \times 10^{-2}$, we find that the peak gain is given by $\sqrt{G_i^{\parallel}G_i^{\perp}} = 1.6 \times 10^{-3}\,(\text{Wm})^{-1}$ as seen in figure 5(a). Note that the slight asymmetry seen in the Brillouin line-shapes are consistent with a small residual contribution from Kerr-induced four-wave mixing [29].

4. Air damping within the photonic lattice

Based on our discussion in section 2, optical forces (that drive the Brillouin-active phonon modes of the system) are only non-vanishing near the core of the HC-PBF. Hence, all of the Brillouin active modes produce appreciable motion of the silica-air matrix. The participation of air in the motion of these modes leads us to expect appreciable change in the Brillouin linewidth as viscous damping of air is eliminated [31–33]. To test this hypothesis (and the interpretation of these signatures as Brillouin-active phonon modes) we place the HC-PBF in a vacuum chamber such that the Brillouin spectra can be obtained with and without air (i.e. under vacuum). The HC-PBF is therefore loosely mechanically spliced to standard single mode fiber on both sides such that there is open access to the HC-PBF by air.

Heterodyne spectroscopy is performed using the all-fiber apparatus seen in figure 6(a). The free-space beamsplitter of our previous apparatus is replaced with a fiber wavelength-division multiplexer, the waveplates by fiber polarization controllers, and the collimators by direct fiber connections. While the additional single-mode fiber in the beam path presents many nonidealities , including a larger FWM background, drift and non-ideal HC-PBF coupling, the linewidth and frequencies of the resonances can be accurately determined for a series of isolated Brillouin-active modes. We use the procedure described in [29] to interpret the measured Fano-like resonances (figure 6(b) inset). Prominent and reproducible peaks are fit and the fit parameters of three

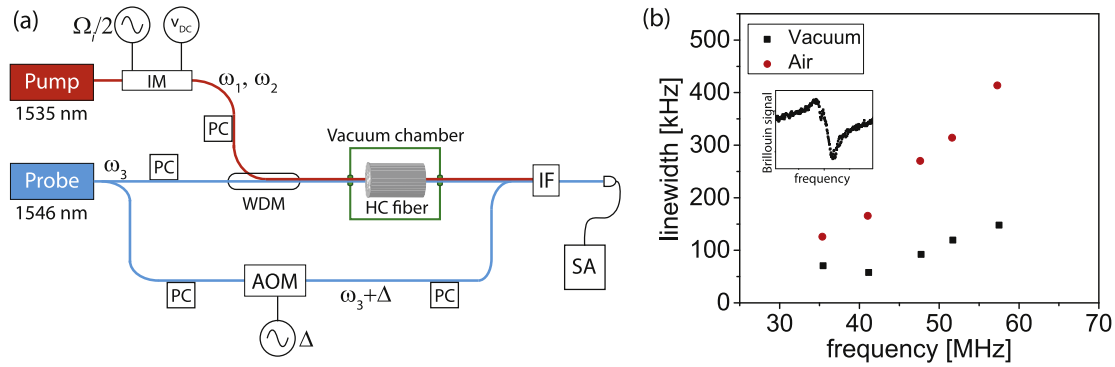

Figure 6. (a) Experimental apparatus with vacuum chamber: IM, intensity modulator; PC, polarization controller; WDM, wavelength-division multiplexer; HC fiber, hollow-core fiber; AOM, acousto-optic modulator; IF, interference filter; and SA, spectrum analyzer. Ω_i is the acoustic resonance frequency. (b) Linewidth versus frequencies for air and vacuum configurations. A single resonance is highlighted in the inset. Note that the Fano-like profile of the Brillouin lineshape is due to the interference with the Kerr four-wave mixing nonlinearity.

traces are averaged, giving their frequency and linewidth (figure 6(b)). This procedure is repeated in both vacuum and air. The result is striking; figure 6(b) reveals a clear (~2.5-fold) linewidth narrowing when the fiber is evacuated. Hence, these measurements strongly support our interpretation of the resonant family of Brillouin-active phonon modes seen in figure 5(a).

5. Simulations

Numerical simulations are developed to further explore the mechanisms behind forward Brillouin scattering in hollow-core PBF, following the methods described in [26, 35]. 2*D* finite element model (FEM) simulations capture the character of acoustic displacement fields that participate in forward Brillouin scattering processes; phase matching requires a vanishing longitudinal wave-vector, meaning that all of the Brillouin active phonon modes are, to a superb approximation, transverse in character. This same 2*D* FEM simulation domain is used to identify the guided optical modes supported by the fiber optic structure. The coupling ($\{G_i\}$) to each Brillouin-active phonon mode ($\{\Omega_i\}$) is readily computed through overlap integrals between the computed optical and phonon displacement field distributions [26].

Note that the accurate specification of the numerous geometrical parameters of the HC-PBF poses a significant challenge. Fortunately, this fiber (HC-1550-02) has been the subject of careful analysis for the purposes of accurate electric field calculations [34]; using the parameters of [34] and through additional discussions with these authors, we accurately specify the hollow-core fiber geometry seen in figure 7(a). The inner two rings of holes (green in figure 7(a)) were adapted directly from scanning electron microscope (SEM) data (or images) provided by the authors of [34]. The remaining geometry (blue in figure 7(a)) is completely specified by three parameters measured in [34]: d from figure 7(f), the hole-to-hole spacing, and the fillet radius of the corners.

By importing the measured fiber cross-section into our COMSOL Multiphysics FEM solver, we obtain the simulation domain seen in figure 7(a); both optical and transverse acoustic modes were simulated using the same simulation domain. The fundamental guided optical modes of HC-PBF fiber were simulated using a 2D mode solver. The field profiles, effective mode index, and group velocity of the computed modes demonstrate good agreement with those computed in [34]. The modal energy densities for two orthogonally polarized modes of this system are shown in figures 7(b), (c). This same simulation domain is used in the structural mechanics module where we solve for the transverse acoustic modes of the 2D hollow-core geometry (figures 7(d), (e)).

While an immense number of phonon modes are supported by this structure, we seek to identify the Brillouin-active phonon modes and their coupling strengths. In what follows, we provide a formal definition for the Brillouin gain coefficients $G_i^{\parallel}$ and $G_i^{\perp}$, and describe the procedure by which they are calculated. We consider guided optical modes at frequencies ω_m and ω_n, expressed as $\mathbf{E}_m^k e^{i(k(\omega_m)z-\omega_m t)}$ and $\mathbf{E}_n^l e^{i(k(\omega_n)z-\omega_n t)}$, where indices k and l denote the polarization state, taking on values of either s or p. These optical waves interact through the ith phonon mode, with a displacement field of the form $\mathbf{u}_i e^{i(K(\Omega_i)z-\Omega_i t)}$; phase-matched coupling is assumed between the interacting fields. Following the treatment in [26], we express the Brillouin gain coefficient

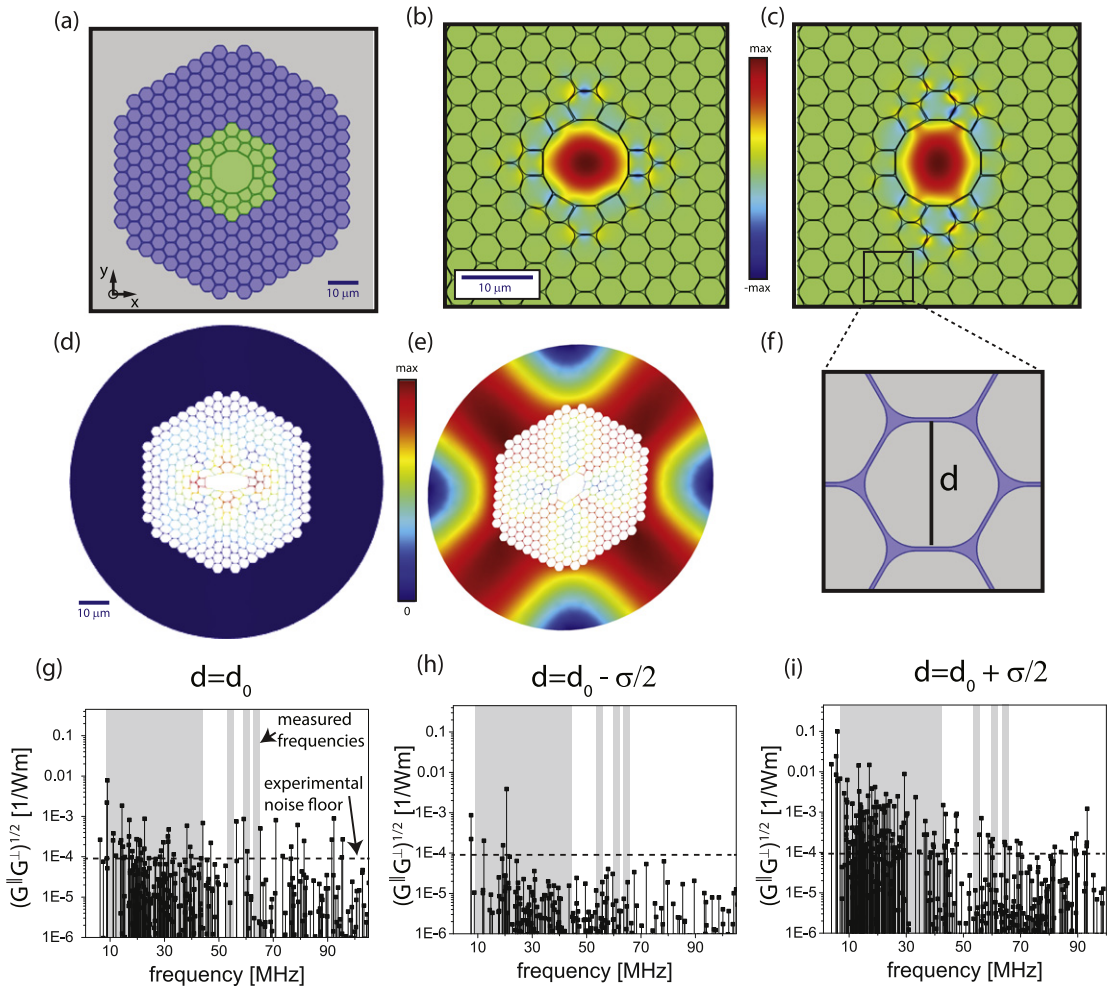

Figure 7. Multi-physics simulations: (a) hollow-core fiber geometry. The green region is defined exactly from a SEM of the fiber and the blue region is defined by three parameters given in [34] and detailed in the text. (b) Calculated x-polarized electric field. (c) Calculated y-polarized electric field. (d) Strong Brillouin-active mesh mode at 9 MHz. (e) First acoustic cladding mode at 7.5 MHz. (f) Geometry used to define the parameters for gain simulations. (g)–(i) Gain calculations with d indicated and given as $d_0 = 3.77$ μm and the standard deviation, σ, given as $\sigma = 84$ nm. A dashed line corresponds to the experimental background and the gray regions correspond to the experimental resonance frequency locations. Parameters: $Q = 200$, $\lambda = 1550$ nm, $p_{11} = 0.1$, $p_{12} = 0.285$, $p_{44} = -0.0925$, $\rho = 2203$ kg m^{-3}, pressure-wave speed is 5996 ms^{-1} and shear-wave speed is 3719.3 ms^{-1} for fused silica.

associated with the ith phonon mode between polarizations l and k as

$$G_i^{kl}(\omega_m, \omega_n) = \frac{2\omega\, Q_i}{\Omega_i^2 v_g^2} \frac{|\langle \mathbf{f}^{kl}, \mathbf{u}_i \rangle|^2}{\langle \mathbf{E}_m^k, \epsilon \mathbf{E}_m^k \rangle \langle \mathbf{E}_n^l, \epsilon \mathbf{E}_n^l \rangle \langle \mathbf{u}_i, \rho \mathbf{u}_i \rangle}. \quad (1)$$

Above, we use the following definitions: ϵ is the transverse dielectric distribution of the fiber, ρ is the transverse mass density distribution, Q_i is the phonon quality factor, ω is the angular frequency of the Stokes wave, $\mathbf{f}^{kl}$ is the complex spatial profile for the time-harmonically varying force density produced by the interference between $\mathbf{E}_m^k$ and $\mathbf{E}_n^l$, as defined in [26], and $\langle \mathbf{A}, \mathbf{B} \rangle$ is a vector inner product, defined as $\langle \mathbf{A}, \mathbf{B} \rangle \equiv \int \mathbf{A} \cdot \mathbf{B}^* \, dx dy$. As in [26], $\mathbf{f}^{kl}$ includes forcing due to electrostriction in the body as well at the boundary, in addition to radiation pressure at the surfaces.

Through numerical treatment of forward Brillouin interactions in the HC-PBF system, we make the following approximations and definitions. Since, $\omega \gg \Omega_i$, to an excellent approximation, we can replace ω with the average of ω_m and ω_n; with this modification, it follows from equation (1) that $G_i^{kl} = G_i^{lk}$. Using this simplification, we define the intra-polarization gain coefficient, $G_i^{\parallel}$, as $G_i^{\parallel} \equiv G_i^{kl}$ where $k = l$; similarly, we define the inter-polarization gain coefficient $G_i^{\perp}$ as $G_i^{\perp} \equiv G_i^{kl}$ where $k \neq l$. Note that the value of G_i^{kk} actually differs slightly depending on electric polarization relative to the complex silica-air matrix. However, through the simulations presented here (and in the appendix), we define $G_i^{\parallel} = G_i^{pp}$ where E_x from figure 7(b) defines the p-polarization, and we make the approximation $G_i^{ss} \approx G_i^{pp}$, as the character of coupling does not change

drastically with polarization state. However, no such approximation is needed for $G_i^{\perp}$, since $G_i^{sp} = G_i^{ps} = G_i^{\perp}$ from our definition above.

Through simulations, the identified Brillouin-active acoustic modes can be cast into two broad categories. The first type have acoustic energy density primarily in the nanoscale silica-air matrix (meshed region) of the fiber (figure 7(d)). These 'mesh-modes' are confined by strong acoustic impedance mismatches by the center hole on the inside and by the solid glass cladding on the outside. These mesh-modes also have varying degrees of spatial localization; some have elastic wave energy that extends throughout the silica-air matrix, and others are highly confined to central region (i.e., first few periods) of the silica-air matrix. The other class of modes extends throughout the silica cladding and the silica-air matrix, as seen in figure 7(e); these are more reminiscent of Brillouin active modes observed in conventional step-index fibers [23, 24].

The forward Brillouin gain is calculated with equation (1) and plotted versus frequency in figure 7(g). As opposed to standard symmetric single-mode fiber, where either $G_i^{\parallel}$ or $G_i^{\perp}$ is zero for each acoustic mode (i.e. the product, $G_i^{\parallel} G_i^{\perp} = 0$), the complexity of the HC-PBF allows for a nonzero product of these gains ($G_i^{\parallel} G_i^{\perp} \neq 0$) for a large range of modes. Note that the simulations shown in figures 7(g)–(i) show the total Brillouin coupling produced by the effects of both radiation pressure and electrostriction. Further analysis (based on these simulation methods) also reveal that electrostriction and radiation pressure have a comparable contribution to photon–phonon coupling for many of the dominant Brillouin-active phonon modes. This contrasts sharply with conventional solid core fibers, where electrostrictive coupling is typically orders of magnitude larger than radiation pressure. In the HC-PBF, surface forces (including radiation pressure) produce appreciable coupling owing to the large ratio of surface areas to volumes within the nanoscale silica-air matrix. The more localized mesh-modes exhibit stronger couplings than the acoustic modes that extend to the outer cladding; these localized mesh-modes more frequently have improved overlap with the optical force distribution, a key requirement for appreciable gain (equation (1)).

Simulations also reveal an incredible sensitivity to the critical dimensions of the HC-PBF cross-section. To elaborate on this point, we explore the effect of a plausible variation in the fiber inner diameter (d) within the standard deviation (σ) of the measured (from [34]) geometric parameters. Three simulations with simulated dimensions $d = \{d_o,\ d_o - \sigma/2,\ d_o + \sigma/2\}$ are shown in figures 7(g)–(i) respectively, revealing dramatic variations in the frequency and strength of the Brillouin resonances. Since this dimensional sensitivity makes one-to-one comparison between theory and experiment challenging; accurate simulation of the Brillouin response would require detailed and exact specifications of the fiber dimensions along its entire length.

To facilitate a qualitative comparison between the Brillouin measurements of figure 5 and the simulations, we indicate the experimental Brillouin sensitivity (horizontal dashed line) and the frequency bands where Brillouin signatures were detected (shaded gray) in figures 7(g)–(i). Detailed comparison between experiment and simulations reveals three notable points of agreement with the experimental data: the bands over which the Brillouin-active phonon modes exist show reasonable agreement, the gain tapers off rapidly at higher frequencies in theory and experiment, and the gain magnitudes are comparable ($\sim 10^{-3}\ \mathrm{W}^{-1}\ \mathrm{m}^{-1}$). While the observed dimensional sensitivity makes the identification of individual Brillouin active phonon modes challenging, it also presents an opportunity to either enhance or suppress photon–phonon coupling through small modifications to the fiber dimensions.

6. Noise considerations

6.1. Spontaneous scattering

Continuing from section 2.2, the spontaneous Brillouin scattering rates can be expressed in terms of the Brillouin gain coefficient. To a superb approximation, growth of spontaneous Stokes and anti-Stokes fields is given by $\mathrm{d}P_2/\mathrm{d}z \cong \mathrm{d}P_3/\mathrm{d}z \cong G_i P_1 N(T)$; here $N(T)$ is a temperature dependent driving term. Again, for intra-polarization scattering $G_i \to G_i^{\parallel}$, and for inter-polarization scattering $G_i \to G_i^{\perp}$. Extending the treatments of [36, 37] to the case of spontaneous forward Brillouin scattering [38], the total spontaneously generated optical power produced by the ith Brillouin active phonon mode is given by

$$P_2^{\,i} \cong P_3^{\,i} \equiv \int S_i(\Omega)\,\mathrm{d}\Omega \cong G_i P_1 L \frac{\pi}{2}\frac{c}{\lambda}\frac{k_B T}{Q_i}. \tag{2}$$

Here, $P_2^{\,i}$ ($P_3^{\,i}$) represents the total spontaneously scattered Stokes (anti-Stokes) power of the ith mode, integrated over the power spectral density ($S_i(\Omega)$), G_i is the stimulated gain coefficient ($G_i^{\parallel}$ or $G_i^{\perp}$), P_1 is the pump power, L is waveguide length, k_B is the Boltzman constant, T is temperature, Q_i is the acoustic quality factor, c is the speed of light, and λ is the optical wavelength. Note that like in backward Brillouin and in Raman scattering, in the limit of very low temperatures $k_B T \to \hbar\Omega_i(\bar{n}_{\mathrm{th}} + 1)$ for Stokes and $k_B T \to \hbar\Omega_i(\bar{n}_{\mathrm{th}})$ for anti-Stokes and we see that $P_2^{\,i}/P_3^{\,i} = e^{\frac{\hbar\Omega_i}{k_B T}}$.

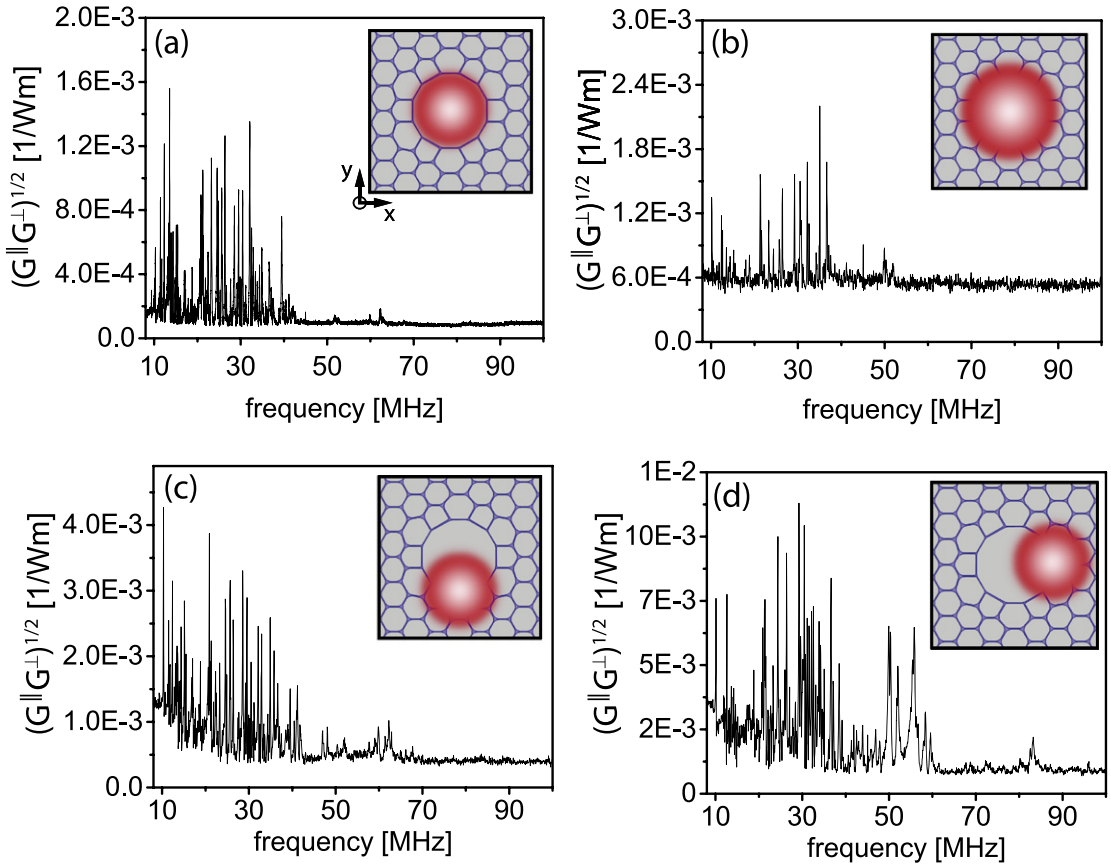

Figure 8. Misaligned Brillouin gain measurements for the (a) ideally coupled case and with the fiber offset by (b) 50 μm in the z-direction (i.e. defocused via motion towards the lens), (c) 5 μm in the y-direction (vertical), and (d) 5 μm in the x-direction (horizontal). The insets in are iconic representations of the implemented offset.

While we measure $\sqrt{G_i^{\|}G_i^{\perp}}$ directly in this work (figure 5), through numerical simulations, we find that $G_i^{\|}$ and $G_i^{\perp}$ have qualitatively similar magnitude and frequency dependence (see appendix) for more information. For an example using equation (2) we can estimate the spontaneous optical scattering rate as follows: considering a single Brillouin active phonon mode with $G_i = 1.6 \times 10^{-3}$ mW^{-1} and $Q_i = 200$, with $P_1 = 100$ mW (or $\sim 10^{18}$ photons per second), $L = 10$ m, $T = 298$ K, and $\lambda = 1550$ nm, the total spontaneously generated power scattered by this phonon mode is given by $P_2 = P_3 = 10$ pW (or $\sim 10^8$ photons per second).

6.2. Non-ideal coupling

In principle, with proper alignment into the core of the HC-PBF, most of the light can be coupled into the fundamental modes. However, HC-PBF fibers are also known to have a class of optical surface modes with a significantly smaller proportion of energy in the core [39]. Moreover, the surface modes have a stronger overlap with the silica-air matrix and might be expected to give rise to larger Brillouin coupling. By misaligning the light from the core, these optical modes can be more strongly populated, thus allowing for the exploration of this effect. Therefore, the depolarized Ph-FWM spectrum is measured after misalignment of the HC-PBF in the three principle directions (figure 8). The measurements reveal an enhancement of similar resonances as well as the addition of gain for new acoustic resonances. Therefore researchers interested in minimizing noise should take sufficient care to couple only into the fundamental mode. Furthermore, if this noise source is of principle concern, the alignment should be optimized while simultaneously measuring the Brillouin noise signature.

7. Discussions and conclusions

Through a combination of experiments and multi-physics simulations, we have shown that hollow core photonic bandgap fiber supports a family of densely spaced Brillouin-active phonon modes below 100 MHz with coupling strengths approaching those of conventional silica fiber. Through this study, we have focused on the physics of photon–phonon coupling in a specific 1550 nm bandgap fiber. While the experimental and

theoretical methods developed here are very general, note that each photonic bandgap fiber structure will have a different Brillouin response. For example, the fiber used in [25] is designed for use at 800 nm and therefore could be expected to have a different response, requiring independent experimental and numerical investigation.

Through these studies, multi-physics simulations provide a window into complex optomechanical interactions with the nanomechanical silica-air matrix. Specifically, simulations permitted us to identify the character of the Brillouin-active phonon modes, and revealed that both radiation pressure and electrostriction contribute to the strong couplings observed here. Through variation of the fiber dimensions (within a standard deviation) we found that the character, strength, and precise locations of the Brillouin active phonon modes can change substantially. This dimensional sensitivity indicates that it may be difficult to make a one-to-one mapping between experiments and theoretically predicted resonances. On the other hand, this incredible sensitivity of the Brillouin spectrum to fiber critical dimensions suggests opportunity for enhancement or suppression of these interactions.

Using the unique symmetry properties of the Brillouin-active phonon modes in the photonic bandgap fiber, we employed an inter-polarization based Ph-FWM process to obtain virtually background free measurement of the Brillouin spectrum. Note that this measurement approach should be effective for the study of a range of fiber geometries [40].

As a complement to these measurements, we also presented relatively comprehensive numerical simulations for intra-polarization (co-polarized) and inter-polarization (depolarized) Brillouin scattering processes (appendix). These cases are of more general interest for both noise properties of fibers and as the basis for stimulated scattering processes. Building on these numerical results, we illustrated how these computed coupling coefficients can be used to estimate the Brillouin induced noise properties of the fiber. Hence, these general results serve as the foundation for the phase- and polarization-noise estimates in hollow-core fiber. Brillouin-based noise properties, of the type discussed in [25] could prove important wherever quantum coherence must be preserved.

Note the numerical simulations presented here were very involved, and quite computationally demanding. Hence, future studies could benefit from a combination of numerical optimization and (or) analytical reductions of the system complexity that make design-space exploration more efficient. This system may be amenable to effective medium treatments in certain limits, as the features of the nanoscale silica mesh are far smaller than the acoustic wavelength in many instances.

Inhomogeneous broadening due to the change in dimensions along the fiber axis is expected to affect the Brillouin process in HC-PBF. In addition to the added complication to modeling the fiber, in a strongly inhomogeneous fiber the effective phonon linewidth will broaden. However, from a practical perspective Brillouin scattering may be useful in measuring certain types of inhomogeneities. Finally, we note that the identified Brillouin interactions may also represent a power limitation for applications, and could be useful for nonlinear optical and sensing applications.

Acknowledgments

Primary support for this work was provided by NSF grant DMR 1119826. The authors thank Nathan Flowers-Jacobs, Anna Kashkanova, Alexey Shkarin and Jack Harris at Yale University for invaluable assistance through the development of the vacuum fiber fixture, Faustin Carter and Dan Prober at Yale University for help with the vacuum chamber, and Kiarash Aghaie and colleagues at Stanford University for sharing data necessary to completely specify the hollow-core fiber geometry.

Appendix. Complete Brillouin gain calculations

For the forward Brillouin processes including spontaneous (figure 3), stimulated (figures 2(a), (b)), and phonon-mediated four-wave mixing (figures 2(c), (d)), there are only three distinct gain coefficients: $G^{\parallel}$, $G^{\perp}$, and $\sqrt{G^{\parallel}G^{\perp}}$. With knowledge of these three coefficients, in addition to equation (2) for the spontaneous case, all of the relevant powers for newly generated frequencies can be calculated. Therefore, for completeness, we present here the simulated coefficient spectrum for $G^{\parallel}$ (figures A1 (a)–(c)), $G^{\perp}$ (figures A1(d)–(f)) and $\sqrt{G^{\parallel}G^{\perp}}$ (figures A1(g)–(i)) for comparison. In addition we include the geometric variations for each case as in figure 7. Note that despite subtle variations in both gain and frequency, the qualitative character the three gain profiles is similar, including order of magnitude and frequency range. Therefore, in general, the qualitative conclusions from experimental results given specifically for $\sqrt{G^{\parallel}G^{\perp}}$ (from figure 5), can be useful for initial estimates for all other forward-Brillouin interactions in the HC-1550-02 hollow-core fiber.

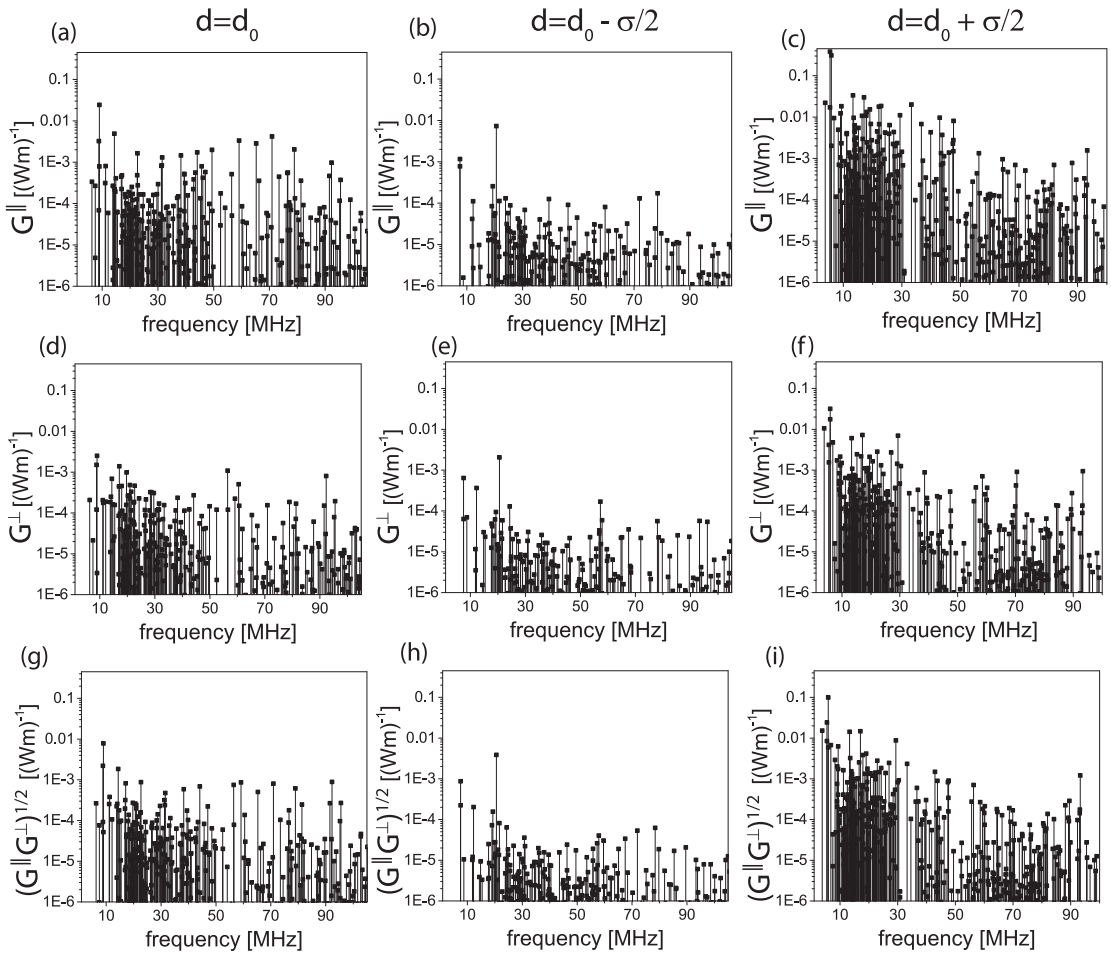

Figure A1. Simulated forward Brillouin gain for the three distinct gain coefficients: (a)–(c) $G^{\parallel}$, (d)–(f) $G^{\perp}$, and (g)–(i) $\sqrt{G^{\parallel}G^{\perp}}$. The geometry is specified by the column label and is defined as in figure 7.

References

[1] Knight J C, Broeng J, Birks T A and Russell P S J 1998 *Science* **282** 1476–8
[2] Cregan R F 1999 *Science* **285** 1537–9
[3] Russell P 2003 *Science* **299** 358–62
[4] Ouzounov D G, Ahmad F R, Muller D, Venkataraman N, Gallagher M T, Thomas M G, Silcox J, Koch K W and Gaeta A L 2003 *Science* **301** 1702–4
[5] Nisoli M, Silvestri S D and Svelto O 1996 *Appl. Phys. Lett.* **68** 2793–5
[6] Couny F, Benabid F and Light P S 2007 *Phys. Rev. Lett.* **99** 143903
[7] Zhong W, Marquardt C, Leuchs G, Andersen U L, Light P, Couuy F and Benabid F 2007 Squeezing by self induced transparency in Rb filled hollow core fibers *Conf. on Lasers and Electro-Optics Europe—Technical Digest* vol 399 p 91058
[8] Ghosh S, Bhagwat A R, Renshaw C K, Goh S, Gaeta A L and Kirby B J 2006 *Phys. Rev. Lett.* **97** 1–4
[9] Light P S, Benabid F, Couny F, Maric M and Luiten A N 2007 *Opt. Lett.* **32** 1323–5
[10] Vogl U, Peuntinger C, Joly N Y, Russell P S, Marquardt C and Leuchs G 2014 *Opt. Express* **22** 29375
[11] Sprague M R, Michelberger P S, Champion T F M, England D G, Nunn J, Jin X M, Kolthammer W S, Abdolvand A, Russell P S J and Walmsley I A 2014 *Nat. Photonics* **8** 287–91
[12] Shelby R M, Levenson M D, Perlmutter S H, Devoe R G and Walls D F 1986 *Phys. Rev. Lett.* **57** 691–4
[13] Corney J F, Drummond P D, Heersink J, Josse V, Leuchs G and Andersen U L 2006 *Phys. Rev. Lett.* **97** 1–4
[14] Poustie A J 1992 *Opt. Lett.* **17** 574–6
[15] Poustie A J 1993 *J. Opt. Soc. Am.* B **10** 691
[16] Bergman K, Haus H A and Shirasaki M 1992 *Appl. Phys.* B **55** 242–9
[17] Elser D, Andersen U L, Korn A, Glöckl O, Lorenz S, Marquardt C and Leuchs G 2006 *Phys. Rev. Lett.* **97** 133901
[18] Dong R, Heersink J, Corney J F, Drummond P D, Andersen U L and Leuchs G 2008 *Opt. Lett.* **33** 116–8
[19] Lorenz S, Silberhorn C, Korolkova N, Windeler R S and Leuchs G 2001 *Appl. Phys.* B **73** 855–9
[20] Milanovic J, Huck A, Heersink J, Marquardt C, Andersen U L and Leuchs G 2007 *Laser Phys.* **17** 559–66
[21] Kang M S, Nazarkin A, Brenn A and Russell P S J 2009 *Nat. Phys.* **5** 276–80
[22] Wang J, Zhu Y, Zhang R and Gauthier D 2011 *Opt. Express* **19** 5339–49
[23] Shelby R, Levenson M and Bayer P 1985 *Phys. Rev.* B **31** 5244–52
[24] Shelby R, Levenson M and Bayer P 1985 *Phys. Rev. Lett.* **54** 939–42
[25] Zhong W E N, Stiller B, Elser D, Heim B, Marquardt C and Leuchs G 2015 *Opt. Express* **23** 27707

[26] Qiu W, Rakich P T, Shin H, Dong H, Soljačić M and Wang Z 2013 *Opt. Express* **21** 31402–19
[27] Wolff C, Steel M J, Eggleton B J and Poulton C G 2015 *Phys. Rev.* A **92** 013836
[28] Fellegara A, Melloni A and Martinelli M 1997 *Opt. Lett.* **22** 1615–7
[29] Shin H, Qiu W, Jarecki R, Cox J A, Olsson R H, Starbuck A, Wang Z and Rakich P T 2013 *Nat. Commun.* **4** 1944
[30] Li M, Pernice W H P, Xiong C, Baehr-Jones T, Hochberg M and Tang H X 2008 *Nature* **456** 480–U28
[31] Starr J B 1990 Squeeze-Film Damping in Solid-State Accelecrometers *Solid-State Sensor and Actuator Workshop* pp 44–47
[32] Tang W 1994 *Proc. IEEE Micro Electro Mechanical Systems An Investigation of Micro Structures Sensors, Actuators, Machines and Robotic Systems* pp 199–204 (http://ieeexplore.ieee.org/lpdocs/epic03/wrapper.htm?arnumber=555623)
[33] Ho C-M and Tai Y-C 1998 *Annu. Rev. Fluid Mech.* **30** 579–612
[34] Aghaie K Z, Digonnet M J F and Fan S 2013 *J. Lightwave Technol.* **31** 1015–22
[35] Rakich P T, Davids P and Wang Z 2010 *Opt. Express* **18** 14439–53
[36] Raymer M G and Mostowski J 1981 *Phys. Rev.* A **24** 1980
[37] Boyd R, Rzaewski K and Narum P 1990 *Phys. Rev.* A **42** 5514–21
[38] Kharel P, Behunin R O, Renninger W H and Rakich P 2015 arXiv:1512.07606
[39] West J A, Smith C M, Borrelli N F, Allan D C and Koch K W 2004 *Opt. Express.* **12** 1485
[40] Wolff C, Steel M J and Poulton C G 2014 *Opt. Express* **22** 32489